A storm-induced flood and associated nearshore dispersal of the river-derived suspended 137Cs

Uchiyama, Yusuke ; Tokunaga, Natsuki ; Aduma, Kohei ; Kamidaira, Yuki ;
Tsumune, Daisuke ; Iwasaki, Toshiki ; Yamada, Masatoshi ; Tadeda,···

A storm-induced flood and associated nearshore dispersal of the river-derived suspended ^{137}Cs

Yusuke Uchiyama [a],*, Natsuki Tokunaga [a], Kohei Aduma [a], Yuki Kamidaira [b], Daisuke Tsumune [c], Toshiki Iwasaki [d], Masatoshi Yamada [e], Yutaka Tadeda [f], Takashi Ishimaru [g], Yukari Ito [g], Yutaka W. Watanabe [h], Ken Ikehara [i], Miho Fukuda [j], Yuichi Onda [k]

[a] Department of Civil Engineering, Kobe University, Kobe, Japan
[b] Nuclear Science and Engineering Center, Japan Atomic Energy Agency, Tokai, Ibaraki, Japan
[c] Sustainable System Research Laboratory, Central Research Institute of Electric Power Industry, Abiko, Japan
[d] Faculty of Engineering, Hokkaido University, Sapporo, Japan
[e] Central Laboratory, Marine Ecology Research Institute, Onjuku, Chiba, Japan
[f] Environmental Science Research Laboratory, Central Research Institute of Electric Power Industry, Abiko, Chiba, Japan
[g] Department of Ocean Sciences, Tokyo University of Marine Science and Technology, Tokyo, Japan
[h] Faculty of Environmental Earth Science, Hokkaido University, Sapporo, Japan
[i] Research Institute of Geology and Geoinformation, National Institute of Advanced Industrial Science and Technology, Tsukuba, Ibaraki, Japan
[j] National Institute of Radiological Sciences, National Institute for Quantum Science and Technology, Chiba, Japan
[k] Center for Research in Isotopes and Environmental Dynamics, University of Tsukuba, Tsukuba, Ibaraki, Japan

HIGHLIGHTS

- A storm-induced coastal dispersal of river-derived suspended ^{137}Cs was investigated.
- In situ core sampling and high-resolution numerical modeling were conducted.
- The riverine ^{137}Cs is primarily distributed near the mouth and the southern coasts.
- Breakwater and coastal structures effectively trap the sedimentary ^{137}Cs.

GRAPHICAL ABSTRACT
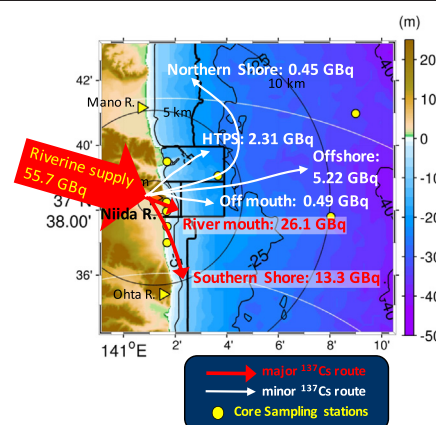
ARTICLE INFO

ABSTRACT

Accidental leakage of radionuclides from the Fukushima Nuclear Power Plant (FNPP1) took place in the aftermath of the catastrophic tsunamis associated with the Great East Japan Earthquake that occurred on March 11, 2011. Significant amount of radionuclides released into the atmosphere were reportedly transported and deposited on land located near FNPP1. The Niida River, Fukushima, Japan, has been recognized as a terrestrial source of highly contaminated suspended radiocesium adhering to sediment particles in the ocean through the river mouth as a result of hydrological processes. Remaining scientific questions include the oceanic dispersal and inventories of the sediments and suspended radiocesium in the ocean floor derived from the Niida River. Complementing limited in situ data, we developed a quadruple nested 3D ocean circulation and sediment transport model in an extremely high-resolution configuration to quantify the transport processes of the suspended

* Corresponding author.
E-mail address: uchiyama@harbor.kobe-u.ac.jp (Y. Uchiyama).

radiocesium. Particularly, we investigated the storm and subsequent floods associated with Typhoon 201326 (Wipha) that passed off the Fukushima coast in October 2013, and subsequently promoted precipitation to a considerable extent and associated riverine freshwater discharge along with sediment outfluxes to the ocean. Using in situ bed sediment core data obtained from regions near the river mouth, we conducted a quantitative assessment of the accumulation and erosion of the sediments and explored the resultant suspended radiocesium distribution around the river mouth and nearshore areas along the Fukushima coast. We identified three major accumulative areas, near the river mouth within an area < 1 km, around the breakwaters in the north of the river mouth, and along the southern coastal area, while offshore and northward transports were minor. The present study clearly exhibits substantial retention of the land-derived radiocesium adsorbed to the sediments in the coastal areas, leading to possible long-term influences on the surrounding marine environment.

1. Introduction

A nuclear accident occurred at the Fukushima Daiichi Nuclear Power Plant (FNPP1. Fig. 1) due to catastrophic tsunamis associated with the Great East Japan Earthquake struck on March 11, 2011. Substantial amounts of radioactive substances were then released into the atmosphere and the ocean (Buesseler et al., 2011; Chino et al., 2011; Kawamura et al., 2011; Yasunari et al., 2011; Kumamoto et al., 2015). Tokyo Electric Power Company (TEPCO, 2012) reported that the main radioactive substances released were ^{131}I, ^{134}Cs, and ^{137}Cs, among which, ^{137}Cs has garnered considerable attention since its half-life is relatively long at 30.1 years and its activity persists over a long period.
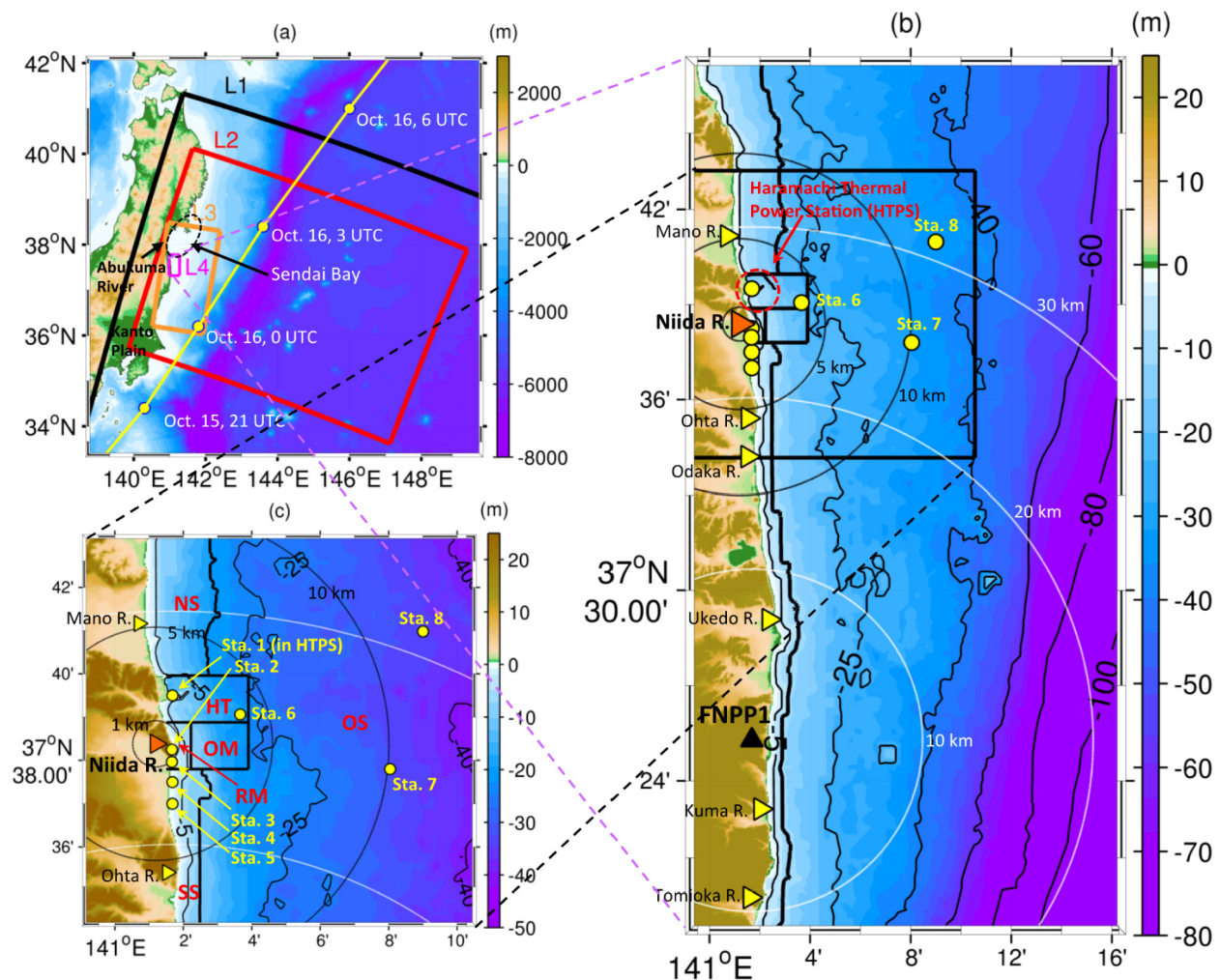

Fig. 1. Geographical maps of the study area. Bluish colors indicate the depths in the ocean (m) and brownish colors indicate terrestrial altitudes (m). (a) Perimeter of the quadruple nested ROMS model areas. Black box: ROMS-L1; red box: ROMS-L2; orange box: ROMS-L3; magenta box: ROMS-L4; and yellow line indicates the best track of Typhoon Wipha connecting the labeled times in UTC. (b) Enlarged view of the entire ROMS-L4 domain. (c) Further enlarged view of the study area near the Niida River mouth. Thick black boxes and lines indicate boundaries of the sub-regions (NS, HT, RM, OM, SS, and OS) used for the inventory analysis in Section 4.4, thin black contours indicate isobaths (m), and thin black and white semi-circles indicate the distances from the Niida River mouth (red triangle marker) and FNPP1 (black triangle marker). Yellow triangle markers correspond to the location of the mouth of the indicated rivers. Yellow circles indicate the stations selected for the core sampling survey (Sta. 1–8).

Radionuclides released into the atmosphere were transported mainly to the northwest region of FNPP1 by the predominant southeasterly wind at the time of the accident, and most radionuclides were deposited on terrestrial areas such as Fukushima and the Kanto Plain (Hirose, 2012; Chartin et al., 2013). In contrast, atmospheric deposition and direct inflow from FNPP1 into the ocean are presumed to be the main pathways for radionuclide entry into the marine environment. Research has been conducted with limited measurement in the early stages of the post-accident aided by application of numerical models to evaluate whether the ocean received 3–6 PBq as the direct release of ^{137}Cs from FNPP1 beginning from March 26, 2011 (Tsumune et al., 2012, 2013; Aoyama et al., 2016b; Buesseler et al., 2017; Kumamoto et al., 2019), while the atmospheric deposition contributed 12–15 PBq to the western north Pacific Ocean out of the total accidental atmospheric release of 15–20 PBq (e.g., Aoyama et al., 2016a, 2016b).

Dissolved ^{137}Cs in the upper ocean initially tends to be transported mainly in the southwestward direction along the coastline located south of FNPP1 (Tsumune et al., 2012). Likewise, concentrations of radionuclides adhering to suspended sediments in water column and marine bed sediments (hereinafter we call them suspended radionuclides or suspended ^{137}Cs) are also observed to be higher on the southern side of FNPP1 than those observed on the northern side (Ambe et al., 2014; Tsumune et al., 2020). However, zooplankton, fish and benthos contaminated with relatively high concentrations of radionuclides have also been observed near the mouth of the Abukuma River in Sendai Bay, located on the northern side of FNPP1 (e.g., Kaeriyama et al., 2015; Narimatsu et al., 2015). The existence of such highly contaminated fauna suggests that river-derived radionuclides exert a substantial influence. Nagao et al. (2013) and Kinouchi et al. (2015) reported that dissolved and suspended radionuclides adsorbed by mineral particles (e.g., clay, silt, and sand) were transported through the rivers at every flood event associated with storms and typhoons, and such radionuclides were eventually discharged into the ocean. The radionuclides derived from rivers strongly depend on the flow rate of rivers and the amount of radioactive materials deposited in catchment areas (Iwagami et al., 2017; Onda et al., 2020; Ueda et al., 2013). Yamashiki et al. (2014) reported that in the Abukuma River basin, approximately 61.4% of the terrestrial radionuclides discharged into the ocean was attributable to the flood events caused by typhoons. Though the concentration of radionuclides in the bed sediments in the Fukushima coast gradually decreased, benthic organisms, fish, and shellfish decreased, and were found to be contaminated with highly radioactive substances immediately after the FNPP1 accident (Tsuboi et al., 2015). This may be true as marine fauna captured in this area show radioactivity that seldom exceeds the regulated value, even as reported in 2021 (Fisheries Agency, 2021).

Although the dissolved radionuclides deposited into the ocean are expected to undergo rapid dilution due to mixing with ambient seawater, the suspended radionuclides may accumulate around the river mouth, and because of settling, they may continue to affect the coastal environment for a long period. Additionally, this process introduces a time lag following the direct release through hydrological processes, because such terrestrial radionuclides mostly undergo attachment with the suspended particles and sediments, which are transported via different mechanisms to the dissolved radionuclides in the water (e.g., Misumi et al., 2014). These suspended radionuclides have been intermittently discharged from the river mouth with the occurrence of infrequent flood events. They recirculate in the ocean as they readily sink to the bottom of the ocean due to settling, and this process is counteracted by resuspension back into the water following an abrupt increase in bed shear stresses. Therefore, suspended radionuclides are anticipated to persist in considerable amounts near the river mouth and coastal areas because of their low mobility, leading to the continuous introduction of radioactivity into ambient water, thereby affecting marine flora and fauna. Therefore, it is extremely important for marine environmental scientists to investigate transport-dispersal-deposition

processes of terrestrial radionuclides supplied from rivers and to understand their underlying mechanisms in the coastal ocean.

The Niida River is a 62.9 km-long minor river, officially categorized as a second-class river maintained municipally, flowing through Fukushima Prefecture with the river mouth located in Minami-Souma approximately 24 km north of the FNPP1. Similar to that observed in the Abukuma River basin, the catchment area is characterized by high terrestrial radioactivity due to the initial atmospheric deposition attributable to the accident (Chartin et al., 2013; Nagao et al., 2015). Hydrological processes have led to the weathering of terrestrial surface sediments that are subsequently gathered in the river channel for transportation downstream, particularly during flood events. In fact, Eyrolle-Boyer et al. (2016) and Naulier et al. (2017) reported that a markedly higher amount of suspended ^{137}Cs than that of dissolved ^{137}Cs flowed out from the Niida River basin after Typhoon 201326 (Wipha). Hence, the Niida River has been recognized as a source of highly contaminated suspended radionuclides that enter the ocean. The total amounts of the deposited ^{137}Cs in the catchment of several rivers near the Niida River were estimated to be 578 TBq for the Abukuma River, 536 TBq for the Ukedo River, while 189 TBq for the Niida River (Sakuma et al., 2019). Therefore, the contribution through river flux from the Abukuma and Ukedo rivers located at north and south of the Niida River may be larger than that from the Niida River.

The primary scientific questions of this study pertained to the extent of suspended radiocesium adhering to sediments released from the Niida River into the ocean by storm-induced flooding, and the possible fate of the river-derived radiocesium in adjacent coastal seas. Therefore, this study aimed to understand the coastal-scale transport processes of particulate matter and to quantify the possible influences of river-derived suspended radionuclides and their inventory in the marginal seas off Fukushima. In addition to in situ observation of the bed sediments, a high-resolution numerical model of transport, dispersal, and deposition of suspended radionuclides derived from rivers is useful for examining the governing dynamic processes in coastal seas. However, such models have not been applied until now with resolution of river mouths of width of O (10–100 m) and their surrounding areas to accurately represent the processes. In previous studies, numerical models have been used to analyze the behavior of suspended radionuclides over an extensive area at coarser horizontal grid resolutions at O (1 km) without considering riverine sediment inputs (Choi et al., 2013; Misumi et al., 2014). Hence, we conducted a two-month numerical hindcast including the storm and flood event associated with Typhoon 201326 (Wipha), that passed off the Fukushima coast in October 2013, using a coupled river-ocean-wave-sediment model along with a static absorption model to assess the amount of radiocesium attached to sediments. The employed 3-D numerical ocean circulation model includes the Regional Oceanic Modeling System (ROMS; Shchepetkin and McWilliams, 2005, 2009) in a quadruple nested configuration (Fig. 1), that enabled the introduction of a lateral model grid spacing of 50 m in the inner-most, finest nested domain, coupled with a 3-D Eulerian multi-size class suspended sediment transport model and a two-layer stratigraphy bed model based on the study reported by Blaas et al. (2007). The iRIC-Nays 2DH river model (Jang and Shimizu, 2005; Shimizu et al., 2014) was used to model the depth-averaged flow and sediment transport in the Niida River. To precisely investigate the bed shear stresses, particularly in nearshore areas, a third-generation spectral wave model, SWAN (Booij et al., 1999), subjected to initialization and enforcement by the operational regional-scale spectral wave analysis of GPV-CWM provided by the Japan Meteorological Agency (JMA), was used. We also performed in situ sampling of bed sediment cores at several locations around the Niida River mouth, immediately after occurrence of the flood event due to Wipha, and compared the results with the model results to assess the reproducibility of the modeled deposition processes of bed sediments around the mouth.

2. Methods

2.1. Core sampling survey

Core sampling of bed sediments for radioactive ^{137}Cs measurement was performed at a total of eight points (Sta.1–8), denoted by using yellow circles in Fig. 1c, in the vicinity of the Niida River mouth after the passage of Typhoon Wipha. Sampling was performed only once at each sampling station, defined as Sta.1 to Sta.5 in the shallow coastal areas and Sta.6 to Sta.8 offshore. Owing to the restriction of met-ocean conditions and logistics, sampling was performed twice in the following manner: at the three offshore stations, Sta. 6–8 on October 18, 2013, two days after the typhoon passed, and at the five coastal stations, Sta.1–5 on October 31, 2013, 15 days after the typhoon passed. The nearshore samples at Sta. 1–5 were collected manually by scuba divers, while those at Sta. 6–8 were collected using a multiple corer obtained from the RV Shinyo-maru of Tokyo University of Marine Science and Technology (Kubo et al., 2020). Sta.1 and Sta.6 are located near the breakwater of the Haramachi thermal power station (HTPS) in the northern part of the Niida River mouth. Sta.1–6 are located within a 5-km area of the river mouth, while Sta.2 and Sta.3 are in the immediate vicinity of the river mouth. The collected sediment cores (Fig. S1) were sliced into 1-cm segments and stored in a freezer at −25 °C. Each slice was used for particle size analysis. The samples were vacuum-dried and placed in U8 containers, and the sedimentary radioactive Cs concentrations were measured using a gamma-ray spectrometer with a coaxial-type Ge detector (GR2018, Canberra Industries Inc., USA, CT; 1.7 keV/ 1.33 MeV resolution and 26% relative efficiency). Data on the concentrations of sedimentary radioactive Cs were then decay-corrected based on the sampling date (Kubo et al., 2020). The results are shown in Table 1.

The sampled cores of the bed sediments are expected to represent the history of past flood events and resultant sedimentological processes, while the bed surface primarily reflects the most recent event. Thus, we computed the inventory I_{nv} of ^{137}Cs attached to the sediments in the cores by integrating ^{137}Cs concentration vertically from the bed surface at $z = -h$ down to z_v (m) mentioned below, as represented by

$$I_{nv} = \int_{-h-z_v}^{-h} \rho_m C_r dz \qquad (1)$$

where ρ_m is dry bulk density of mixed-size sediments in the bed (kg/ m^3), C_r is particulate ^{137}Cs concentration (Bq/kg), h is local water depth (m), and z_v is the depth (m) at which C_r reaches a value of zero. We should consider z_v to represent samples collected from sufficiently deep regions, whereas $z_v=0.1$ (m) is assumed to compensate for the limitation of the shallowest core sample. Consequently, the inventory I_{nv} (Bq/kg) represents the total amount of particulate ^{137}Cs in the bed sediment per unit area of the seafloor at each core sampling station.

2.2. Experimental design

In the present study, we used the two-month hindcast result of the inner-most ROMS-L4 model, which contains 32 vertical s-layers and a horizontal resolution of 50 m, encompassing an area of approximately 25 km × 50 km, including the Niida River mouth, FNPP1, and the core sampling stations (Fig. 1b). This model is based on a quadruple nested ROMS driven by the JCOPE2 reanalysis (Miyazawa et al., 2009) using an offline one-way nesting technique (Marchesiello et al., 2003; Mason et al., 2010; Uchiyama et al., 2018a). The JCOPE2-ROMS system has been extensively used in various studies and exhibits high reproducibility on coastal seas located around Japan (Kamidaira et al., 2017, 2018, 2019; Kurosawa et al., 2020; Masunaga et al., 2018, 2019; Tada et al., 2018; Takeda et al., 2021; Uchiyama et al., 2017b, 2018a–c; Zhang et al., 2019). The model is further coupled with a multi-size-class non-cohesive suspended sediment transport model with a two-layered bed stratigraphy model (Blaas et al., 2007; Kamidaira et al., 2021) that additionally accounts for wave effects evaluated by a third-generation spectral wave model SWAN (Booij et al., 1999; Cao et al., 2018). A static absorption of ^{137}Cs to sediment particles was evaluated with the empirical formula (He and Walling, 1996) modified for the study area (Golosov et al., 2017; Murota et al., 2016; Qin et al., 2012; Takata et al., 2015, 2020). Riverine sediment supply was quantified for the Niida River with the iRIC-Nays2DH river model (Jang and Shimizu, 2005; Nelson et al., 2016; Shimizu et al., 2014, 2019), which computes depth-integrated river flow, associated multi-grain-size sediment transport, bed morphology evolution, and bank erosion in rivers (Iwasaki et al., 2015). Details of the exploited numerical models are described in Appendix in Supplemental Data. The analysis period included the flood event associated with Typhoon 201326 (Wipha), which was the closest to the study area on October 16, 2013 (Fig. 1a). Realistic surface wind, waves, swells, barotropic and baroclinic tides, freshwater inputs from rivers, large-scale currents through the open boundaries, suspended sediments and associated ^{137}Cs from the Niida River, and fine-resolution coastal topography and bathymetry were all considered in the ROMS-L4 model (Section A.1). The model provided data on a temporal evolution of surface elevation, 3-D currents, water density (temperature and salinity), concentration of suspended sediments (sand, silt, and clay), bed stratigraphy, and sedimentary suspended ^{137}Cs in the coastal ocean around the Niida River mouth.

We investigated two experimental cases using the ROMS-L4 model. Case 1 is the baseline case used for most of the subsequent analyses, which represents realistic sediment transport processes in the ocean without the presence of Niida River-derived sediments. Three size classes of the sediments, namely sand, silt, and clay (Table S2), were considered in Case 1. Case 2 involved the introduction of two more sediments (silt and clay) discharged from the Niida River as additional prognostic variables to eventually compute a total of five sediments. The river-derived sand information was ignored in Case 2 because the

Table 1
Results of the core sampling survey. Listed below are the latitude and longitude coordinates of each sampling station, dates of the samplings conducted, local water depth of the stations h, the Euclidean distance from the Niida River mouth (D_{NR}) and FNPP1 (D_{FI}). Surface[137]Cs: near-bed surface ^{137}Cs attached to the sediments averaged over the depths of 0 to 1 cm from the bed surface (Bq/kg), Inventory: the total amount of ^{137}Cs per unit area integrated vertically from the bed surface down to 10 cm (Bq/m^2), and d_{50}: median grain size of the near-bed surface sediments.

Sta	Latitude	Longitude	Date	Depth	D_{NR}	D_{FI}	Surface [137]Cs	Inventory	d_{50}
	(°N)	(°E)		h (m)	(km)	(km)	(Bq/kg)	(Bq/m^2)	(μm)
1	37.658	141.025	10/31/2013	5	2.39	26.7	67.04	11,616	182
2	37.638	141.028	10/31/2013	5	1.76	24.5	27.17	9,055	231
3	37.633	141.027	10/31/2013	7	1.42	23.4	17.73	3,502	231
4	37.625	141.025	10/31/2013	5	1.41	23.4	4.21	2,581	372
5	37.617	141.025	10/31/2013	5	2.39	22.3	3.39	955	260
6	37.651	141.061	10/18/2013	25	5.0	27.0	104.0	66,155	86
7	37.630	141.134	10/18/2013	35	10.0	25.0	5.9	865	371
8	37.630	141.150	10/18/2013	30	12.0	31.0	5.2	1,108	87

contribution of sand to suspended ^{137}Cs was found to be only 2% of the total in Case 1, while introducing nontrivial numerical delicacy. Hence, the Case 2 model is based on the omission of a mixture of the Niida River-derived sediments with the initially distributed bed sediments to distinguish dispersal of the Niida River-supplied sediments from that of the bed sediments.

3. Met-ocean conditions and resultant sediment transport

Typhoon 201326 (Wipha) commenced near the Mariana Islands at 12:00 UTC on October 10, 2013, and intensified into a Category 4 typhoon with a minimum pressure of 930 hPa. It advanced toward the northwest region, then veered to the east, while maintaining its intensity, and traveled further north with acceleration (Fig. 1a). The typhoon was sufficiently intense to be classified as a once-in-a-decade storm when it approached and landed in the Kanto region of Japan. Typhoon Wipha weakened as it skirted Japan's eastern coastline on October 15, while leading to considerable precipitation. It also spawned a massive landslide on Izu-Oshima Island. On October 16, Wipha passed through the north region of the island before dawn, and then subsided into an extratropical cyclone off Sanriku at 15:00 on the east coast of the Boso Peninsula.

The met-ocean data shown in Fig. 2 clearly demonstrate the prominent influence of Typhoon Wipha during the analysis period. When Wipha was closest to the study area on October 16, wind speed increased to approximately 20 m/s, wave height reached approximately 4.6 m, and the associated heavy precipitation induced the most substantial discharge of approximately 180 m³/s at the Niida River mouth, followed by the occurrence of two minor floods for several days thereafter. Sediments were discharged into the ocean from the Niida River, with floods peaking during the typhoon. High frequency variability

dominated the surface current velocity due to tides and diurnal wind fluctuations, while low-frequency signals were also visible. The low-frequency currents and wind were approximately SSW parallel to the coastline. On the other hand, during the mild climate following the typhoon, the surface current and wind were relatively weak and developed in the opposite direction, NNE, parallel to the coastline.

Fig. 3 shows examples of the horizontal distribution of the Case 1 results. On October 16 (Fig. 3a), when the typhoon was closest to the study area, the surface currents (horizontal velocity of the topmost grid cells) were prevailed by the overall southward drift and were markedly enhanced near the river mouth regions, including those of the Niida River, as well as around the coastline bends, and near the harbor structure (breakwaters) of HTPS located north of the Niida River mouth. Near HTPS, the prevailing southward coastal currents bypassed the north breakwater and intensified within a few kms off the tip of the structure. On the northern side (Mano River) and the southern side (Ohta River) of the Niida River, the coastal currents veered eastward to form offshore flow due to the influence of the floods. On the contrary, on November 30 (Fig. 3b), during a calm period, the surface currents were noticeably weaker than those observed during the storm. The prevailing direction turned to NNE. The two month-averaged surface currents (Fig. 3c) were like those recorded on October 16, suggesting that the impact of the flood event of the typhoon was significant during the study period. The results clearly showed that the coastal structures, the river discharge, and near-mouth topography modified the nearshore current field substantially. In contrast, the near-bed currents (horizontal velocity of the bottom-most grid cells) formed in a different manner from the surface currents, particularly, in shallow waters during mild climate conditions. The two month-averaged near-bed currents were headed toward WNW that compensated for the surface currents. This implied that vertical recirculation occurred near
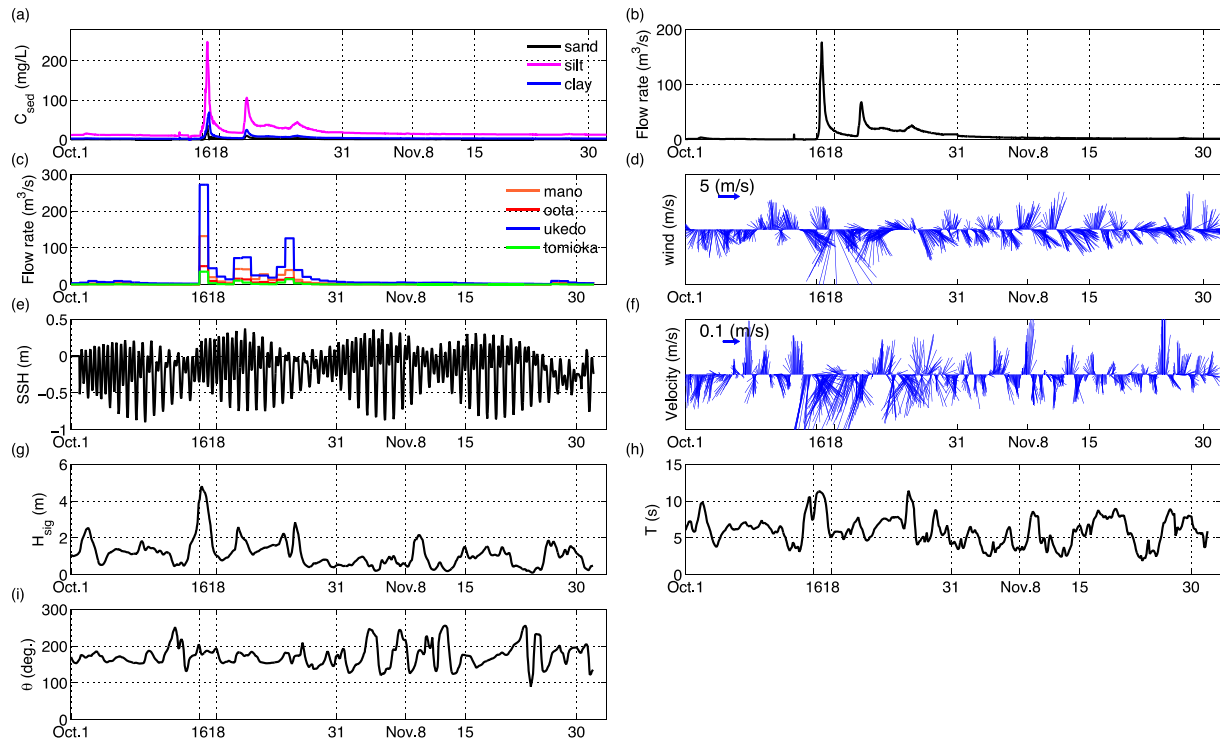

Fig. 2. Meteorological and oceanic conditions near the Niida River mouth from October 1 to November 30, 2013. Typhoon Wipha was observed to be the closest to the study area at around noon on October 16, JST. (a) Niida River-derived suspended sediment concentrations (mg/L) of three size classes (sand, silt, and clay) at the river mouth, (b) hourly freshwater discharge at the Niida River mouth in m³/s, (c) daily freshwater discharge in m³/s at the mouths of four selected adjacent rivers, namely Mano, Ohta, Ukedo, and Tomioka Rivers (Fig. 1) computed by using the HYDREEM run-off model, (d) wind velocity (m/s) at 10 m above the surface at 141.04°E and 34.6405°N, 1 km off the Niida River mouth (same for e–i) based on the GVM-MSM atmospheric analysis, (e) sea surface height (SSH, m), (f) ocean surface current velocity (m/s), (g) significant wave height (m), (h) significant wave period (s), (i) mean wave direction (degree) measured counter-clockwise from the east, where (a) and (b) are obtained by using the iRIC-Nays 2DH river model, (e)-(f) are derived from the ROMS-L4 model (Case 1), and (g)–(i) are derived from the SWAN wave model.
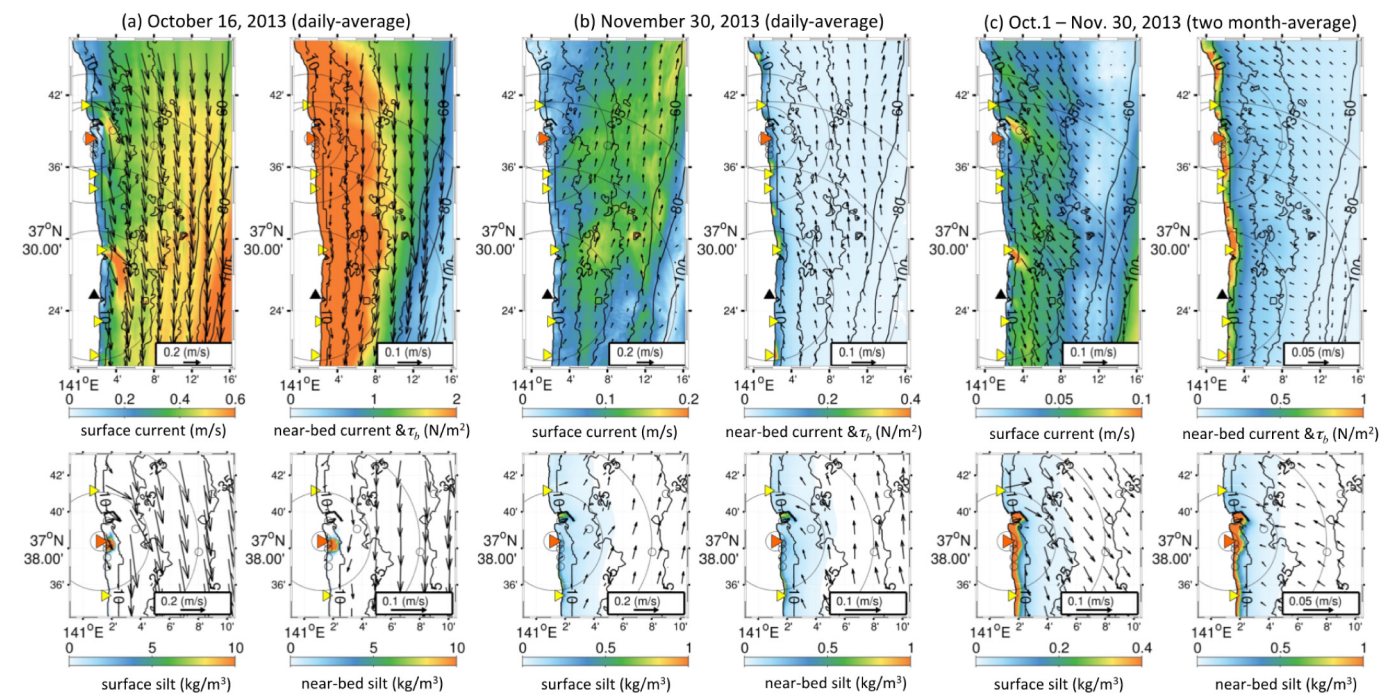
Fig. 3. Results of the numerical model. Displayed variables include (a) daily average for October 16 when the typhoon was observed to be the closest (the stormy condition), (b) daily average for November 30, six weeks after occurrence of the typhoon (a mild condition), and (c) time average for the entire two-month analysis period (the mean condition). In each of the conditions from (a)-(c), upper left panel indicates surface current velocity vectors with their magnitude (m/s) in color, lower left panel indicates surface velocity vectors with surface silt concentration (kg/m³) in color near the Niida River mouth, upper right panel indicates near-bed current velocity vectors with the bed shear stresses (N/m²) in color, and lower right panel indicates near-bed current velocity vectors with near-bed silt concentration (kg/m³) in color near the Niida River mouth. Notice vectors are subsampled. The upper panels indicate results derived from Case 1, while the lower panels indicate results derived from Case 2.

the shore to provoke a coastal upwelling mode. However, depth-dependent horizontal currents were less evident on October 16 owing to intensive vertical mixing associated with the storm.

When the typhoon passed, the bed shear stress considerably increased over the study area as compared to that observed on November 30. The bed shear stress τ_b was extremely high, especially in coastal waters shallower than approximately 35 m isobaths attributable to the strong influence of the waves. Over extensive areas, τ_b reaches a value of 2.0 N/m², which is remarkably greater than the critical shear stress τ_{cr} of sand (i.e., 0.15 N/m²; Table S2) that is considered the most immobile sediment in the model. Hence, resuspension and erosion occurred prominently in all three sediment classes in the entire shallow waters. In contrast, on November 30, τ_b was reduced to a value of 0.1 N/m² overall, whereas it exceeded a value of 0.2 N/m² in the nearshore areas shallower than 10-m isobaths. The two month-averaged τ_b was qualitatively similar in its spatial patterns to those documented on November 30, but to a greater degree. A high τ_b is formed periodically at intervals of approximately 10 to 16 km in the alongshore direction, where the coastline is shaped concave to the offshore (e.g., at 37°24′N, 37°34′N and 37°41′N near the shore).

Silt was the main contributor to the Niida River-derived sediments (Fig. 2a). A significant amount of riverine silt was distributed mostly near the river mouth on October 16 (Fig. 3a). On November 30, the silt underwent considerable dilution near the river mouth, settled near the shore, and dispersed broadly offshore by approximately 25-m isobaths. A certain amount of the river-derived silt exists in the breakwaters of the HTPS and along the coastline on the southern side of the Niida River mouth. On the other hand, silt concentrations are rather less along the coastline on the northern side of the HTPS and in deep ocean. The silt is distributed similarly in the surface and bottom layers, although the near-bed concentrations are generally higher than those near the surface because of vertical settling and resuspension from the

bed. This suggests that the silt settles rapidly upon discharge from the Niida River mouth. Nevertheless, the spatial distributions of the silt differ on a daily basis, which eventually results in the meridionally biased silt distributions extending to the south in the period-averaged silt distributions. This finding implied that the river-derived silt was mainly transported southward and deposited on the southern shores, leading to increased silt concentration in the water by enhanced τ_b and resultant resuspension due to waves.

4. Core sampling vs. model

4.1. History of past flood events and grain size effects on ^{137}Cs

Fig. 4a illustrates the comparison of the bed surface ^{137}Cs, which is activity concentration of ^{137}Cs in the surface 1 cm of the bed sediment, with the inventory I_{nv} (Section 2.1). The inventory is viewed as a record of the history of past flood events and associated deposition on the seafloor. By contrast, the surface ^{137}Cs would largely correspond to deposition of the suspended ^{137}Cs derived from the Niida River by the most recent flood event attributable to Typhoon Wipha. A highly positive correlation with a correlation coefficient of 0.89 is found between the ^{137}Cs inventory and the surface ^{137}Cs. This finding clearly indicated that the suspended ^{137}Cs transport processes and accompanying deposition on the bed during Typhoon Wipha occurred quite similarly to those having occurred with the previous storm and flood events in the past two and a half years after the occurrence of the FNPP1 accident. Both inventory I_{nv} and surface ^{137}Cs values are greater at Station 1 located in HTPS, Sta. 6 off the tip of the breakwater of HTPS, and at Sta. 2 and 3 near the Niida River mouth than those observed at the other stations, though Station 6 demonstrates the maximum values. It should be noted that I_{nv} of Sta. 6 is larger than the average, and this station has a smaller contribution of the latest event to the cumulative inventory.
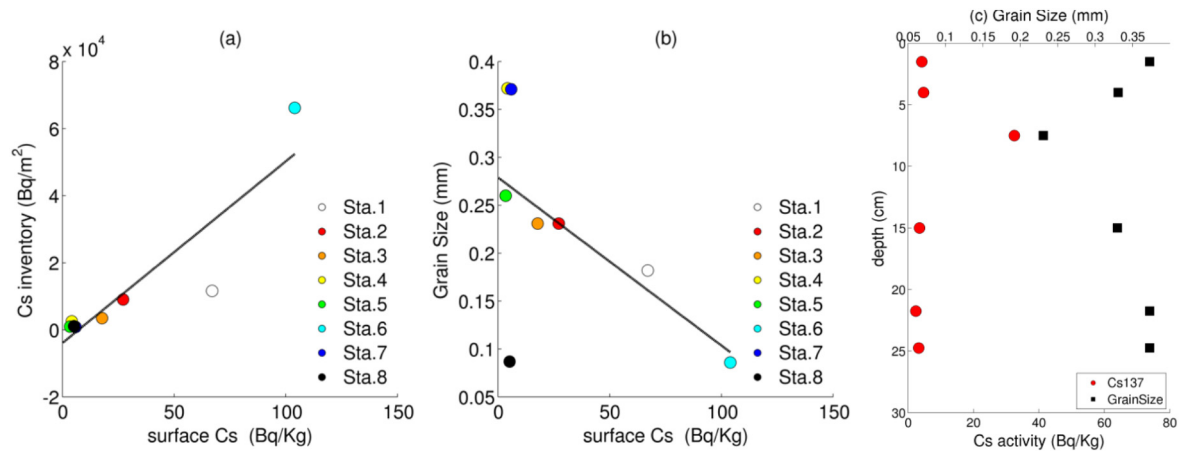
Fig. 4. Results of the core sampling survey. Scatter diagrams of the bed surface ^{137}Cs (Bq/kg) against (a) the inventory I (Bq/m^2) and (b) median grain size (mm) of the surface sediments at each sampling station, Sta. 1–8 (see Fig. 1c for the geographical locations), depicted by using different colors in the legend. (c) An example of the vertical distributions of the median grain size (mm, black square marks) and the suspended ^{137}Cs concentration (Bq/kg, red circles) at each sliced layer in the core sampling data at Sta. 4, where the ordinate indicates the downward distance (depth, m) from the bed surface.

On the other hand, I_{nv} and the surface ^{137}Cs values are less at Sta. 4 and 5 on the southern side of the mouth and Sta. 7 and 8 offshore. Nevertheless, ^{137}Cs is finite yet small even at remote sites such as Sta. 5 and 8, which implies that riverine sediments and suspended ^{137}Cs may be reachable.

It is well known that radionuclides are readily adsorbed on materials with small particles sizes such as clay or silt (Comans and Hockley, 1992; Nakao et al., 2009). Owing to the chemical influences of surface tension and electrification of suspended particles, the extent of adsorption of ^{137}Cs is proportional to the specific surface area, which is the surface area per unit volume, $\{4\pi(d/2)^2\}/\{4\pi(d/2)^3/3\} = 6/d$, for spherical particles. Thus, the smaller the particle size, the more ^{137}Cs is absorbed. Therefore, it is important to examine the transport and deposition processes of particles by size to precisely evaluate the transport of suspended ^{137}Cs particles. As shown in Table 1 and Fig. 4b, the median grain size d_{50} of the surface sediments at the eight sampling sites ranged broadly between 86 μm (silty) and 372 μm (sandy). Finer-grained sediments were found offshore at Sta.6 and 8, while coarser-grained sand was predominant at offshore Sta. 7. Nearshore d_{50} at Sta. 1–5 shows an evident sandy nature ranging between 182 and 372 μm, with an overall increasing trend in d_{50} from north to south directions.

Fig. 4c shows an example of the vertical distribution of d_{50} and ^{137}Cs in the core sampled at Station 4, located in the southern region of the Niida River mouth. An apparent negative correlation was found with a correlation coefficient of −0.93. The subsurface d_{50} minimum was observed at 7.5 cm below the bed surface where ^{137}Cs peaks, which were most likely attributed to the past flood events before Typhoon Wipha. In turn, horizontal correlations were not markedly clear, whereas d_{50} and ^{137}Cs concentration of the bed surface sediments exhibited overall inverse proportionality with the correlation coefficient of −0.59 (Fig. 4b). Moreover, the correlation coefficient of the nearshore Sta.1–5 was −0.74, demonstrating that the suspended ^{137}Cs discharged from the Niida River coarsened and was diluted as the particles traveled from the river mouth.

The results of the core sampling survey showed that sedimentary ^{137}Cs was largely related to the particle size with complexity in their spatial distribution, owing to the 3-D transport of the river-derived and marine bed-originated sediments driven by spatiotemporally varying coastal currents and associated deposition processes. Therefore, in the subsequent subsections, the model results have been utilized to examine the hydrodynamics and sediment transport processes by focusing on the contributions of two factors, namely the bottom shear stress that preconditions resuspension on the seafloor, and the sediment budget that determines local erosion and sedimentation to elucidate the mechanism responsible for the ^{137}Cs distribution around the Niida River mouth.

4.2. Bed shear stress for resuspension and deposition

The combined wave-current bed shear stress τ_b in Eq. (A2) changes according to the bottom stress due to the phase-averaged near-bed flow and bottom stress due to the wave orbital velocity on the seafloor. When $\tau_b < \tau_{cr}$, where τ_{cr} is the prescribed critical shear stress depending on the grain size d_{50} of the mixed bed, sediments in the seawater are deposited on the seafloor at the corresponding vertical settling velocity w_s (Table S2). On the contrary, when $\tau_b \geq \tau_{cr}$, the bed sediments are re-suspended in the seawater. Thus, it can be inferred that the smaller the d_{50} value, the smaller the τ_{cr}value and the sedimentation rate. Accordingly, resuspension occurs even at smaller $\tau_b$values, that is, under less energetic bottom currents and waves, for finer sediments.

Fig. 5a–d (top row) shows the modeled bed shear stress τ_b and near-bed velocity vectors for Case 1 overlaid with the observed median grain size d_{50} of the surface sediments in Table 1. The monthly mean τ_b for a non-typhoon period, spanning from November 1–30 (Fig. 5a), is intensified in shallow waters (the local depth $h < 10$ m) along the coast where the wave action on the bottom is significant, but is small offshore. Moreover, τ_b is weak in the sheltered area inside the HTPS and in the vicinity of the Niida River mouth, where the observed d_{50} also tends to be small. Particularly, τ_b near river mouths may be affected by the following two competing processes: 1) convergence of shoreward-propagating waves refracted over the shallow terrace topography of the mouth, and 2) wave amplification by the offshore flow from the river and by wave shoaling on the terrace (Uchiyama et al., 2010, 2017a). The former mechanism is anticipated to promote convergent sediment accumulation near the river mouths, while the latter may enhance the wave-induced stress τ_w to result in more resuspension (Blaas et al., 2007). The model results suggest that the former mechanism is superior to the latter near the mouths of the Niida and Mano rivers located north of the HTPS. Thus, τ_b was reduced and accumulation of finer sediments occurred, while the latter mechanism might be predominant near the Ohta River mouth at a region approximately 5 km south of the Niida River.

On the day of occurrence of maximum flood (Fig. 5b), an intense southward bottom velocity formed near the river mouth. The associated
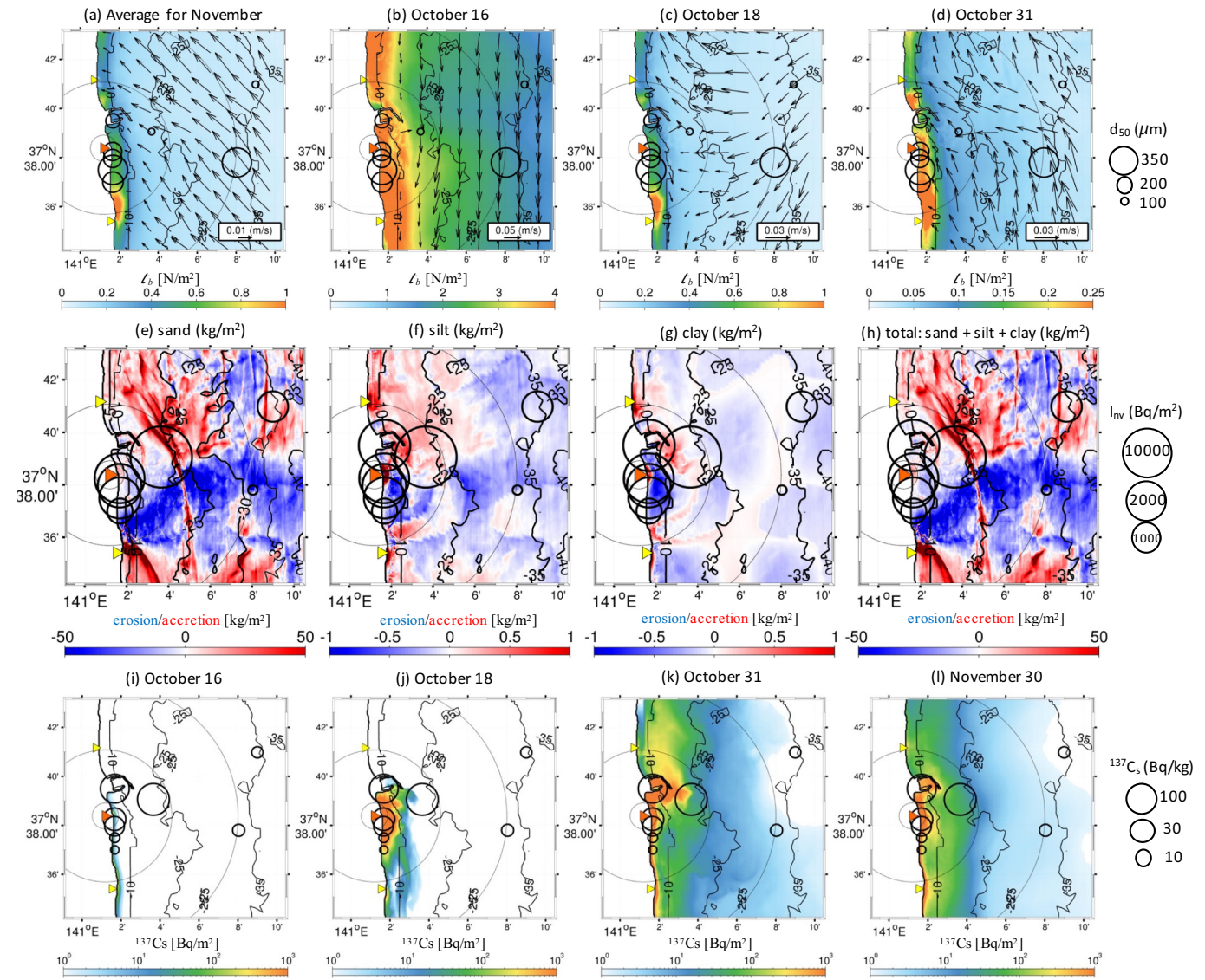
Fig. 5. Top row (panels a–d): Enlarged views of the modeled bed shear stress τ_b and (subsampled) near-bed velocity vectors around the Niida River mouth for Case 1 overlaid with the observed median grain size d_{50} of the surface sediments in Table 1 depicted by using open circles with the variable diameter proportional to d_{50}. (a) Monthly averages for November 2013 as a representative of the no-typhoon conditions, and daily-averaged values for (b) October 16 under the maximum typhoon influences, (c) October 18, two days after occurrence of the typhoon when the survey was conducted at Sta. 6–8, and (d) October 31, 15 days after the typhoon passed when the core samples were collected at the Sta. 1–5. Middle row (panels e–h): Modeled (Case 1) cumulative deposition (accretion, reddish colors) and resuspension (erosion, bluish colors) integrated since October 1 until October 31, 2013, for (a) sand, (b) silt, (c) clay, and (d) a sum of the three-size classes per unit bottom area in kg/m². The overlaid open circles indicate the observed inventory I_{nv} of the bed-core ^{137}Cs (Table 1). Bottom row (panels i–l): The temporal evolution of modeled suspended ^{137}Cs in the marine bed sediments of the two size classes (silt and clay, Case 2) derived from the Niida River (colors, Bq/m²). Daily averaged radioactivity in unit bed area has been depicted for October 16 (Wipha was closest), October 18 (reflecting influences of heavy precipitation associated with Wipha), October 31 (two weeks after Wipha), and November 30 (six weeks after Wipha). The open circles indicate the concentration of measured bed surface ^{137}Cs.

τ_b was extensively high near the shore including the mouth areas, exceeding the critical shear stress τ_{cr} of the least mobile sand class sediments (0.15 N/m²; Table S2) everywhere including the offshore areas deeper than 35 m. This suggests that resuspension and erosion prevailed for all sizes of sediments at all observation sites when the typhoon passed. Two days later, when the offshore sampling was conducted at Sta. 6 to 8, the near-bed velocity was observed to be north-westward with a small τ_b in general (Fig. 5c). All sediments could be deposited at the offshore sampling sites, Sta. 6 to 8, because τ_b was smaller than 0.15 N/m². The median grain size d_{50} at Sta. 6 and Sta. 8 was small in accordance with a small τ_b, whereas Sta. 7 showed an exceptionally considerable d_{50} even at a small τ_b. On October 31, when the nearshore sampling at Sta. 1 to 5 was conducted, the oceanic conditions were extremely mild, and bottom currents

and τ_b were largely diminished (Fig. 5d). Nearshore τ_b was as high as 0.25 N/m² in the southern coastal waters, but reduced to approximately 0.1 N/m² near the Niida River mouth and around HTPS. At Sta. 1 within HTPS and Sta. 2–3 located near the Niida River mouth, d_{50} was found to be finer with smaller τ_b than that recorded at Sta. 4 and 5 located to the south. Hence, nearshore τ_b and d_{50} were moderately correlated.

4.3. Sediment budget analysis

The bed shear stress τ_b indicates the resuspension potential at the bed of interest, whereas the bed evolves due to 3-D sediment transport over time. Hence, we conducted a sediment budget analysis to estimate erosion and accumulation of bed sediments by considering the

divergence and convergence of depth-integrated lateral sediment fluxes of the j-th size class, as expressed by the following equation:

$$\frac{\partial}{\partial t}\int_{-h}^{\eta} c_j dz + \nabla_h \int_{-h}^{\eta} c_j \mathbf{u}_h dz = E_j - D_j, \qquad (2)$$

where η is free surface elevation (m), $\nabla_h = (\partial/\partial x, \partial/\partial y)$ is the horizontal gradient operator, and $\mathbf{u}_h$ is the horizontal velocity vector (m/s). Notably, we deduced the following equation for bed evolution:

$$\frac{\partial S_j}{\partial t} = \rho_{sj}(1 - \lambda)\frac{\partial h_{bj}}{\partial t} = D_j - E_j, \qquad (3)$$

where S_j is vertical downward sediment flux of the j-th class deposited on (positive) or eroded from (negative) the unit seafloor area (kg/m^2/s), ρ_{sj} is the dry density of the j-th sediment (Table S2), h_{bj} is deviation of the seafloor height (m) due only to the j-th sediment measured upward from the initial bed at $z = -h$. The time integral of S_j represents the total amount of sediment accumulated on the bed owing to the lateral sediment transport over time. Likewise, the sum of h_{bj} over j is thus the resultant bed height deviation measurable in situ. Note that h_b is omitted as $h_b \ll H$ ($H = h + \eta$ is total depth in m) in Eq. (2).

Fig. 5e–h (middle row) illustrates the comparison of the modeled cumulative S_j integrated over the month of October 2013 from the Case 1 result with the observed radiocesium inventory I_{nv} (Table 1 and Fig. 4). Overall, I_{nv} of sedimentary ^{137}Cs is substantial where deposition is dominant (reddish color), while it is small in the erosive area (bluish color). Particularly, the offshore area of the breakwater of HTPS centered at Station 6, which is characterized by higher ^{137}Cs, finer d_{50}, and smaller τ_b (Fig. 5a–d), is accretive even though it is far from the Niida River mouth. The reddish accretive area of silt and clay (Fig. 5f, g) extends from the northern area to the southeast region toward Sta. 6 along the HTPS breakwater, demonstrating that lateral transport and the resultant deposition of finer silt and clay play an important role in the accumulation of suspended ^{137}Cs. Indeed, the time-averaged surface velocity for the two months (Fig. 3c), which considerably affects the overall silt and clay transport, shows offshore currents along the breakwater of HTPS to reach Sta. 6. Therefore, the accretive area of fine sediments was formed by the weak bed shear stress under the influence of horizontal transport from the north of the HTPS.

It is worthwhile to quantify the extents of erosion and accretion caused by storm events. As the erosion at Sta. 2–5 ranges from −40 to −50 kg/m^2 (Fig. 5h), it is translated into the thickness of the eroded bed sediments of 2–3 cm, considering the porosity of 0.4 and the sediment density of 2650 kg/m^3. Similarly, the accretion around Sta. 6 was evaluated to be approximately not more than 1 cm in thickness. Therefore, the present storm-flood event caused centimeter-scale bed thickness changes near the river month. This finding also supports the argument made in Section 4.1, which states that only the sediments present in the top few centimeters of the sampled cores may reflect the present event (Fig. 4c) and the lower portions represent a record of past events.

4.4. ^{137}Cs inventory in bed sediments

Fig. 5i–l (bottom row) shows the temporal evolution of suspended ^{137}Cs adhering to the bed sediments derived from the Niida River (colors, Bq/m^2) along with the in situ ^{137}Cs inventory (open circles, Table 1). The modeled ^{137}Cs distributions were then spatially integrated in the offshore direction and in the alongshore direction at 500-m intervals to depict histograms (Fig. 6a–e). Note that for the present analysis, we considered results of Case 2, in which the sediments derived from the Niida River were separately computed from the bed sediment data, enabling us to extract information on the riverine suspended ^{137}Cs contributions.

When the typhoon passed (October 16, Fig. 5i), the river-derived ^{137}Cs was distributed only in the southern nearshore shallow areas by

the prevailing southward sediment transport (Figs. 3a and 5b). Two days later, on October 18 (Fig. 5j), a significant amount of ^{137}Cs was deposited near the mouth with a radius of approximately 2 km. The north-westward transport (Fig. 5c) promoted near-mouth accretion, entrainment in the HTPS harbor facility, and offshore transport toward Sta. 6. In turn, the suspended ^{137}Cs from the Niida River did not reach Sta. 7 and 8 by October 18 when core sampling was conducted. Hence, the in-situ data collected at Sta. 7 and 8 might not fully reflect the influence of Wipha. Subsequently, ^{137}Cs was gradually transported mainly to the south and offshore (Oct. 31 and Nov. 30, Fig. 5k–l) with peaks located at 6–7 km south of the river mouth (Fig. 6a–e). A substantial amount of ^{137}Cs was also transported southward beyond −10 km. Owing to the occasional supply of ^{137}Cs by two small floods occurring after the typhoon (Fig. 2a), the overall ^{137}Cs concentration in the marine bed increased until October 31, whereas it was widely dispersed mainly in the southern and offshore directions by November 30. Northward transport was found mostly near the river mouth, which peaked at approximately 2 km by October 31 (Fig. 6c), albeit to a much lesser degree than the southward transport.

To quantify the regional transport and resultant redistribution of the inventory of river-derived suspended ^{137}Cs absorbed into the bed sediments, we categorized the ROMS-L4 domain into seven segments, as shown in Fig. 1b and c, where the ^{137}Cs inventory was calculated based on the results obtained for Case 2 (Fig. 6f and Table 2). Data on the suspended ^{137}Cs had been derived from the Niida River (NR) by 32.0 GBq until Oct. 18, 2 days after the typhoon passed, and by approximately 55.7 GBq as of Nov. 30. The suspended ^{137}Cs was significantly deposited within approximately 1 km of the river mouth, n.b., in the RM subregion, accounting for 46.8% (approximately 26.1 GBq) of the river supply on November 30. On the other hand, ^{137}Cs deposited in OM, the offshore of RM by approximately 3.5 km from the river mouth, rapidly increased in a few days since the occurrence of the main flood; however, the inventory was extremely small, i.e., only approximately 0.51 GBq as of Oct. 18. The ^{137}Cs in OM then gradually reduced to approximately 0.49 GBq by Nov. 30, which is merely ~1.8% of the inventory in RM. Nearshore-suspended ^{137}Cs transport in the regions shallower than 10 m are strongly biased toward the south (SS). As of Nov. 30, approximately 13.3 GBq exists in the SS, which corresponds to 23.8% of the supplied ^{137}Cs from the Niida River, whereas NS receives only nearly 0.45 GBq. However, the near-mouth area around HTPS labeled HT is highly accretive and receives approximately 9.1 GBq (17.4%) of the river supply due to sediment depositions induced by the breakwater as of October 31. The outflow to the offshore area (OS) is nearly 5.22 GBq (9.36% of the supply), and the outflow to the distant area outside the computational domain (OD) is approximately 7.90 GBq (14.2% of the supply).

5. Discussion

The model results showed that the river-derived suspended ^{137}Cs (NR) attributable to the flood associated with Typhoon Wipha provided nearly 32 GBq within two days. The supplied suspended ^{137}Cs were prominently deposited in the vicinity of the river mouth (RM) by approximately 47%, even though 1.5 months had elapsed after occurrence of the typhoon-induced flood. The offshore mouth area (OM), spanning from 1 km to 3.5 km from the mouth, was not substantially affected by the riverine ^{137}Cs, accounting for only 0.03%–0.75% of the river supply. The increased ^{137}Cs concentration that was reported at the river mouth, and at the interface between the river and the ocean, was consistent with the field measurement conducted by Kakehi et al. (2016). Their work showed that >80% of the river-derived suspended ^{137}Cs from the Abukuma River, located further north of the present study site, was deposited at the river mouth. These results demonstrate that the river-induced suspended ^{137}Cs flux is less dispersive and is thus barely transported to regions located far offshore. Such a near-mouth accumulation may be maintained by the landward near-bottom
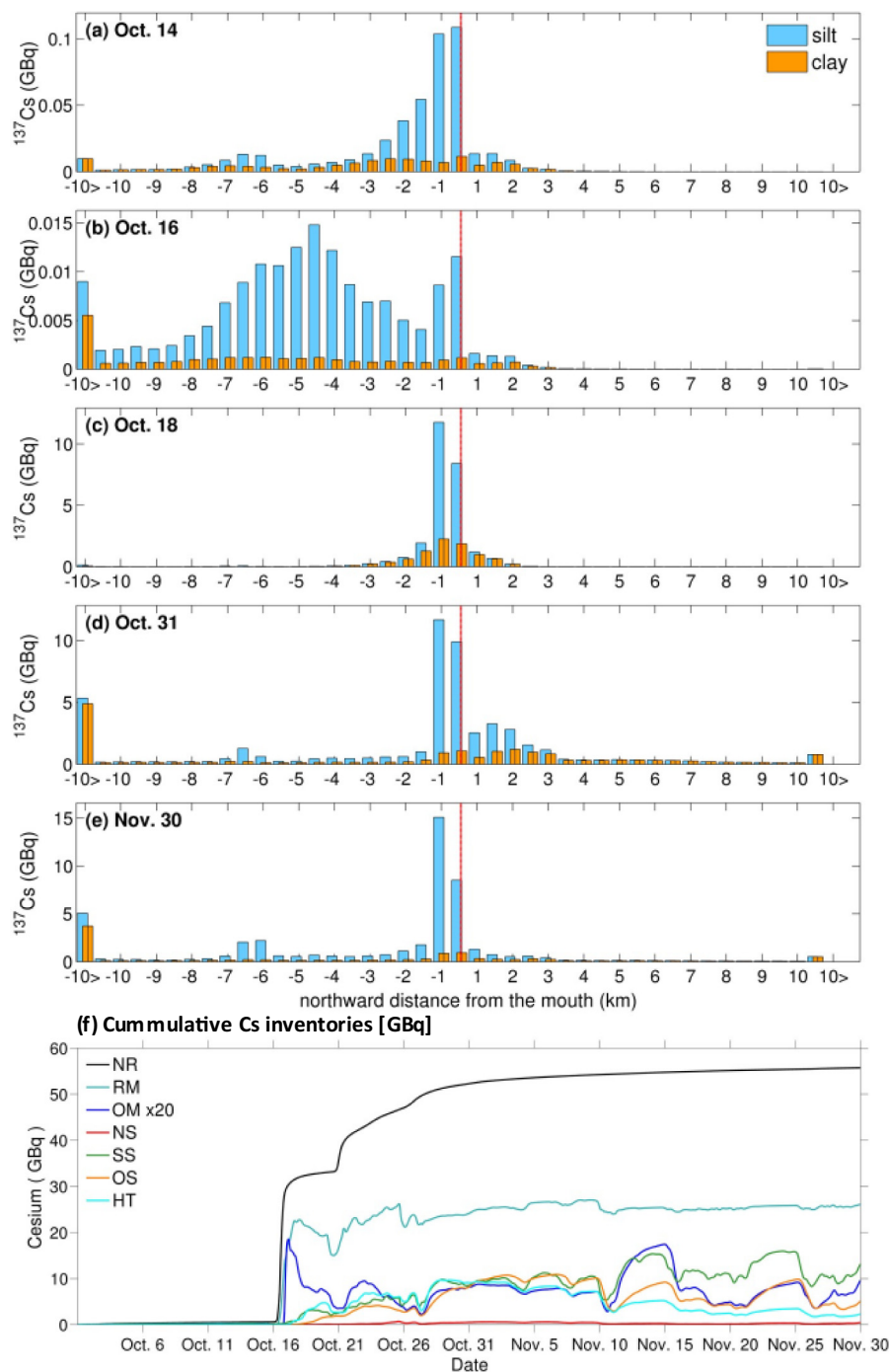
Fig. 6. (a–e) The histogram of sedimentary ^{137}Cs attached to the Niida River-derived silt (cyan) and clay (orange), integrated in the offshore direction and at 500-m alongshore distance intervals (Case 2). The abscissa indicates the northward distance from the Niida River mount shown by the vertical red line. Notice different scales in the ordinate. (f) Time series plot of the ^{137}Cs inventory in the bed sediments in the six subregions defined in Fig. 1b and c and NR: the amount of ^{137}Cs supplied from the Niida River. The displayed acronyms are as follows: RM, the river mouth region within approximately 1 km; OM, offshore of RM as far as approximately 3.5 km (note that the ^{137}Cs in OM is magnified by a factor of 20); NS, the northern shore areas; SS, the southern shore areas; OS, the offshore area deeper than approximately 10 m; and HT, the area around Haramachi Thermal Power Station (HTPS).

transport (Fig. 5a–d), which is formed in the near-bed lower layer to compensate for the near-surface offshore freshwater outflow from the river.

Nevertheless, our results further illustrate the importance of alongshore ^{137}Cs transport in shallow nearshore areas. Figs. 5i–l and 6 show that highly contaminated suspended ^{137}Cs is deposited along the southern coast (SS) and near the breakwater of HTPS in the north of the river mouth (HT). The former is promoted by the predominant southward

^{137}Cs transport due to the southward alongshore currents by the storm, while the latter is attributed to the northwestward bottom currents formed under ordinary, mild oceanic and atmospheric conditions (Fig. 5a–d). However, the northward ^{137}Cs transport is significantly affected by the coastal structure, that is, the HTPS breakwaters located in the north of the river mouth. The breakwaters are generally constructed to shelter the port facility (HTPS) from incoming waves as well as sediment influxes. Apparently, the latter functions as intended.

Table 2
The suspended ^{137}Cs inventory in the bed sediments in the six segments (RM, OM, NS, HT, SS, and OS. See Fig. 1 for the definition). NR: the amount of suspended ^{137}Cs adhering to the sediments supplied from the Niida River, and OD: the suspended ^{137}Cs flowed out of the model domain. The listed ^{137}Cs inventory is expressed in GBq and integrated in time since Oct. 1 until at 0:00 UTM on the labeled day.

Date until	NR	RM	OM	NS	HT	SS	OS	OD
Oct. 14	0.530	0.282	0.004	2.50×10^{-5}	0.028	0.150	0.011	0.056
Oct. 16	0.578	0.026	2.13×10^{-4}	8.20×10^{-6}	0.035	0.130	0.002	0.417
Oct. 18	32.0	22.7	0.514	8.84×10^{-6}	1.11	1.71	0.120	5.79
Oct. 31	52.3	24.2	0.409	0.491	9.08	8.51	8.23	1.42
Nov. 30	55.7	26.1	0.489	0.450	2.31	13.3	5.22	7.90

Thus, the suspended ^{137}Cs is considerably accumulated within, and on the southern side of the HTPS, while further northward ^{137}Cs transport is hampered.

Another important finding is that the suspended ^{137}Cs from the Niida River is observed mostly as silt fraction, proportional to the silt-associated sediment flux from the river (Fig. 2a), rather than sand (not shown) and clay (Fig. 6a–e). As the vertical settling velocity and the resuspension rate of silt are intermediate compared to those of sand and clay (Table S2), silty ^{137}Cs is dispersed more extensively than sandy ^{137}Cs, although markedly less mobile than clayish ^{137}Cs, to accumulate near the source area (i.e., the Niida River mouth). Additionally, based on the significant correlation between the surface ^{137}Cs and the amount of ^{137}Cs inventory of the sampled cores (Section 4.1, Fig. 4), the present model results, such as those pertaining to lateral dispersal and deposition patterns, would be applicable to other storm-induced flood events that have occurred near the Niida River mouth since the FNPP accident. Therefore, we hypothesize that the river-derived suspended ^{137}Cs may have prominently accumulated within 1 km of the river mouth (RM), in the southern beaches (SS), and around the HTPS breakwaters at each flood event.

The radiocesium concentrations in marine fish species off the Fukushima coast have decreased significantly as dissolved ^{137}Cs content in seawater has decreased rapidly since the occurrence of the accident (Buesseler, 2012). However, time-series trends of radiocesium concentrations have been shown to differ among taxa, habitats, and spatial distributions (Wada et al., 2013). The present model did not account for the desorption of suspended ^{137}Cs. In reality, suspended ^{137}Cs deposited near the river mouth or along a coast persist for a long period, as the half-life is approximately 30.1 years. Such accumulated suspended ^{137}Cs particles may leach into seawater and affect the marine environment as dissolved ^{137}Cs. In fact, the Fisheries Agency reported on January 31, 2019, that a common skete (*Raja kenojei*), a species of ray, caught off the Fukushima coast had ^{137}Cs with values exceeding the Japanese standard limit of 100 Bq/kg. This was the first time that marine fauna with an exceeded ^{137}Cs value was captured in four years. As common sketes inhabit the bottom of the sea, they are affected by suspended ^{137}Cs adhering to the bed sediments. Therefore, the evaluation of the distribution of suspended ^{137}Cs in the seabed is a crucial step toward the protection of marine ecosystems from radionuclides.

6. Conclusions

This study investigated the regional transport and resultant deposition of sediments and associated suspended ^{137}Cs on the seabed, derived from the Niida River, Fukushima, Japan. The catchment of this river was found to be contaminated by the initial atmospheric deposition of radionuclides following the FNPP1 accident that occurred in March 2011. We focused on storm-induced flood events associated with Typhoon 201326 (Wipha) in October and November 2013. In situ core sampling data were collected immediately after the typhoon passed, and a high-resolution downscaling numerical model based on the JCOPE2-ROMS system was used to examine the detailed processes and their underlying mechanisms.

The core sampling data revealed that highly contaminated suspended ^{137}Cs were distributed on the seafloor near the Niida River mouth and the breakwater of the adjacent thermal power station (HTPS). A negative correlation between ^{137}Cs concentration and median grain size of the bed surface sediments was identified; the finer the bed sediments, the more ^{137}Cs was absorbed. The inventory of suspended ^{137}Cs particles, viz. the vertically integrated bed sedimentary ^{137}Cs, was positively correlated with the bed surface ^{137}Cs. The ^{137}Cs inventory reflects the history of past storm or flood events occurring since the FNPP1 accident, whereas the surface ^{137}Cs predominantly represents occurrence of the most recent event due to Typhoon Wipha. The significant correlation implies that the transport and deposition processes due to Wipha are like those of previous storms occurred in the past two and a half years since the accident.

On the other hand, the model enables examination of the dynamics and mechanisms underlying sediment transport. Concrete and remarkable consistencies were found between the in-situ grain size and the modeled bed shear stress, and between the observed bed surface ^{137}Cs and the modeled sediment erosion/accumulation. Overall, finer particles accumulate to increase content of the suspended ^{137}Cs in regions where the bed shear stress is lower. However, the horizontal current field is largely affected by the vertical recirculation occurring due to the near-surface freshwater outflow from the river mouth and by the coastal structure of the adjacent HTPS, leading to the establishment of a hot spot of high ^{137}Cs content (e.g., at Sta. 6). Furthermore, the model results (Case 2) were utilized to conduct an inventory analysis of the river-derived suspended ^{137}Cs present in the sea floor. A significant amount of ^{137}Cs was deposited within an area approximately 1 km of the river mouth (RM), near the HTPS breakwater north of the river mouth (HT), and along the coast south of the river mouth (SS). In contrast, a small amount of suspended ^{137}Cs was transported and deposited offshore of the river mouth (OM) and along the coast north of the river mouth (NS). In summary, the present study demonstrates substantial retention of the land-derived radiocesium adhering to the sediments in the shallow coastal areas near the river mouth, leading to possible long-term influences of ^{137}Cs on the surrounding marine environment.

CRediT authorship contribution statement

Yusuke Uchiyama: Conceptualization, Methodology, Supervision, Software, Writing – review & editing, Funding acquisition. **Natsuki Tokunaga:** Investigation, Software, Validation, Visualization, Writing – original draft. **Kohei Aduma:** Investigation, Software, Validation, Visualization. **Yuki Kamidaira:** Investigation, Software, Validation. **Daisuke Tsumune:** Investigation, Methodology, Supervision. **Toshiki Iwasaki:** Methodology, Validation, Software. **Masatoshi Yamada:** Investigation, Methodology, Supervision, Funding acquisition. **Yutaka Tadeda:** Investigation, Formal analysis. **Takashi Ishimaru:** Investigation, Formal analysis. **Yukari Ito:** Formal analysis. **Yutaka W. Watanabe:** Formal analysis, Visualization. **Ken Ikehara:** Formal analysis, Visualization. **Miho Fukuda:** Formal analysis. **Yuichi Onda:** Investigation, Methodology, Supervision, Funding acquisition.

Declaration of competing interest

Acknowledgments

Appendix A. Supplementary data

Supplementary data to this article can be found online at https://doi.org/10.1016/j.scitotenv.2021.151573.

References

Ambe, D., Kaeriyama, H., Shigenobu, Y., Fujimoto, K., Ono, T., Sawada, H., Saito, H., Miki, S., Setou, T., Morita, T., Watanabe, T., 2014. Five-minute resolved spatial distribution of radiocesium in sea sediment derived from the Fukushima Dai-ichi Nuclear Power Plant. J. Environ. Radioact. 138, 264–275. https://doi.org/10.1016/j.jenvrad.2014.09.007.

Aoyama, M., Hamajima, Y., Hult, M., Uematsu, M., Oka, E., Tsumune, D., Kumamoto, Y., 2016a. 134Cs and 137Cs in the North Pacific Ocean derived from the March 2011 TEPCO Fukushima Dai-ichi Nuclear Power Plant accident, Japan. Part one: surface pathway and vertical distributions. J. Oceanogr. 72 (1), 53–65. https://doi.org/10.1007/s10872-015-0335-z.

Aoyama, M., Kajino, M., Tanaka, T.Y., Sekiyama, T.T., Tsumune, D., Tsubono, T., Hamajima, Y., Inomata, Y., Gamo, T., 2016b. 134Cs and 137Cs in the North Pacific Ocean derived from the March 2011 TEPCO Fukushima Dai-ichi nuclear power plant accident, Japan. Part two: estimation of 134Cs and 137Cs inventories in the North Pacific Ocean. J. Oceanogr. 72 (1), 67–76. https://doi.org/10.1007/s10872-015-0332-2.

Blaas, M., Dong, C., Marchesiello, P., McWilliams, J.C., Stolzenbach, K.D., 2007. Contin. Shelf Res. 27 (6), 832–853. https://doi.org/10.1016/j.csr.2006.12.003.

Booij, N.R.R.C., Ris, R.C., Holthuijsen, L.H., 1999. A third-generation wave model for coastal regions: 1. Model description and validation. J. Geophys. Res. Oceans 104 (C4), 7649–7666. https://doi.org/10.1029/98JC02622.

Buesseler, K.O., 2012. Fishing for answers off Fukushima. Science 338 (6106), 480–482. https://doi.org/10.1126/science.1228250.

Buesseler, K., Aoyama, M., Fukasawa, M., 2011. Impacts of the Fukushima nuclear power plants on marine radioactivity. Environ. Sci. Technol. 45 (23), 9931–9935. https://doi.org/10.1021/es202816c.

Buesseler, K., Dai, M., Aoyama, M., Benitez-Nelson, C., Charmasson, S., Higley, K., Maderich, V., Masqué, P., Morris, P.J., Oughton, D., Smith, J.N., 2017. Fukushima Daiichi–derived radionuclides in the ocean: transport, fate, and impacts. Annu. Rev. Mar. Sci. 9, 173–203. https://doi.org/10.1146/annurev-marine-010816-060733.

Cao, Y., Dong, C., Uchiyama, Y., Wang, J., Yin, X., 2018. Multiple-scale variations of wind generated wave in the Southern California Bight. J. Geophys. Res. Oceans 123 (12), 9340–9356. https://doi.org/10.1029/2018JC014505.

Chartin, C., Evrard, O., Onda, Y., Patin, J., Lefèvre, I., Ottlé, C., Ayrault, S., Lepage, H., Bonté, P., 2013. Tracking the early dispersion of contaminated sediment along rivers draining the Fukushima radioactive pollution plume. Anthropocene 1, 23–34. https://doi.org/10.1016/j.ancene.2013.07.001.

Chino, M., Nakayama, H., Nagai, H., Terada, H., Katata, G., Yamazawa, H., 2011. Preliminary estimation of release amounts of 131I and 137Cs accidentally discharged from the Fukushima Daiichi Nuclear Power Plant into the atmosphere. J. Nucl. Sci. Technol. 48 (7), 1129–1134. https://doi.org/10.1080/18811248.2011.9711799.

Choi, Y., Kida, S., Takahashi, K., 2013. The impact of oceanic circulation and phase transfer on the dispersion of radionuclides released from the Fukushima Daiichi Nuclear Power Plant. Biogeosciences 10, 4911–4925. https://doi.org/10.5194/bg-10-4911-2013.

Comans, R.N.J., Hockley, D.E., 1992. Kinetics of cesium sorption on illite. Geochim. Cosmochim. Acta 56 (3), 1157–1164. https://doi.org/10.1016/0016-7037(92)90053-L.

Eyrolle-Boyer, F., Boyer, P., Garcia-Sanchez, L., Métivier, J.M., Onda, Y., De Vismes, A., Cagnat, X., Boulet, B., Cossonnet, C., 2016. Behaviour of radiocaesium in coastal rivers of the Fukushima Prefecture (Japan) during conditions of low flow and low turbidity–

insight on the possible role of small particles and detrital organic compounds. J. Environ. Radioact. 151 (1), 328–340. https://doi.org/10.1016/j.jenvrad.2015.10.028.

Fisheries Agency, 2021. Results of the monitoring on radioactivity level in fisheries products. [Internet] [cited 2021 October 9]. Available fromFisheries Agency. https://www.jfa.maff.go.jp/e/inspection/index.html.

Golosov, V., Botavin, D., Konoplev, A., Wakiyama, Y., 2017. Transformation of different reaches of the Niida River (Japan) after extreme flood. 19 (1), 75–87. https://doi.org/10.21094/rg.2017.006.

He, Q., Walling, D.E., 1996. Interpreting particle size effects in the adsorption of 137Cs and unsupported 210Pb by mineral soils and sediments. J. Environ. Radioact. 30 (2), 117–137. https://doi.org/10.1016/0265-931X(96)89275-7.

Hirose, K., 2012. 2011 Fukushima Dai-ichi Nuclear Power Plant accident: summary of regional radioactive deposition monitoring results. J. Environ. Radioact. 111, 13–17. https://doi.org/10.1016/j.jenvrad.2011.09.003.

Iwagami, S., Onda, Y., Tsujimura, M., Abe, Y., 2017. Contribution of radioactive 137Cs discharge by suspended sediment, coarse organic matter, and dissolved fraction from a headwater catchment in Fukushima after the Fukushima Dai-ichi Nuclear Power Plant accident. J. Environ. Radioact. 166 (3), 466–474. https://doi.org/10.1016/j.jenvrad.2016.07.025.

Iwasaki, T., Nabi, M., Shimizu, Y., Kimura, I., 2015. Computational modeling of 137Cs contaminant transfer associated with sediment transport in Abukuma River. J. Environ. Radioact. 139, 416–426. https://doi.org/10.1016/j.jenvrad.2014.05.012.

Jang, C.-L., Shimizu, Y., 2005. Numerical simulation of relatively wide, shallow channels with erodible banks. J. Hydraul. Eng. 131 (7), 565–575.

Kaeriyama, H., Fujimoto, K., Ambe, D., Shigenobu, Y., Ono, T., Tadokoro, K., Okazaki, Y., Kakehi, S., Ito, S., Narimatsu, Y., Nakata, K., Morita, T., Watanabe, T., 2015. Fukushima-derived radionuclides 134Cs and 137Cs in zooplankton and seawater samples collected off the Joban-Sanriku coast, in Sendai Bay, and in the Oyashio region. Fish. Sci. 81 (1), 139–153. https://doi.org/10.1007/s12562-014-0827-6.

Kakehi, S., Kaeriyama, H., Ambe, D., Ono, T., Ito, S.I., Shimizu, Y., Watanabe, T., 2016. Radioactive cesium dynamics derived from hydrographic observations in the Abukuma River Estuary,Japan. 153, 1–9. https://doi.org/10.1016/j.jenvrad.2015.11.015.

Kamidaira, Y., Uchiyama, Y., Mitarai, S., 2017. Eddy-induced transport of the Kuroshio warm water around the Ryukyu Islands in the East China Sea. Contin. Shelf Res. 143, 206–218. https://doi.org/10.1016/j.csr.2016.07.004.

Kamidaira, Y., Uchiyama, Y., Kawamura, H., Kobayashi, T., Furuno, A., 2018. Submesoscale mixing on initial dilution of radionuclides released from the Fukushima Daiichi Nuclear Power Plant. J. Geophys. Res. Oceans 123 (4), 2808–2828. https://doi.org/10.1002/2017JC013359.

Kamidaira, Y., Kawamura, H., Kobayashi, T., Uchiyama, Y., 2019. Development of regional downscaling capability in STEAMER Ocean prediction system based on multi-nested ROMS model. J. Nucl. Sci. Technol. 56 (8), 752–763. https://doi.org/10.1080/00223131.2019.1613269.

Kamidaira, Y., Uchiyama, Y., Kawamura, H., Kobayashi, T., Otosaka, S., 2021. A modeling study on the oceanic dispersion and sedimentation of radionuclides off the coast of Fukushima. J. Environ. Radioact. 238–239, 106724. https://doi.org/10.1016/j.jenvrad.2021.106724.

Kawamura, H., Kobayashi, T., Furuno, A., In, T., Ishikawa, Y., Nakayama, T., Shima, S., Awaji, T., 2011. Preliminary numerical experiments on oceanic dispersion of 131I and 137Cs discharged into the ocean because of the Fukushima Daiichi Nuclear Power Plant disaster. J. Nucl. Sci. Technol. 48 (11), 1349–1356. https://doi.org/10.1080/18811248.2011.9711826.

Kinouchi, T., Yoshimura, K., Omata, T., 2015. Modeling radiocesium transport from a river catchment based on a physically based distributed hydrological and sediment erosion model. J. Environ. Radioact. 139, 407–415. https://doi.org/10.1016/j.jenvrad.2014.07.022.

Kubo, T., Tanabe, K., Ito, Y., Ishimaru, T., Otsuki, M., Arakawa, H., Watanabe, Y.W., Miura, H., Tsumune, D., Kanda, J., 2020. Changes in radioactive cesium concentrations from 2011 to 2017 in Fukushima coastal sediments and relative contributions of radioactive cesium-bearing microparticles. Mar. Pollut. Bull. 161 (B), 111769, 7 pp. https://doi.org/10.1016/j.marpolbul.2020.111769.

Kumamoto, Y., Aoyama, M., Hamajima, Y., Murata, A., Kawano, T., 2015. Impact of Fukushima-derived radiocesium in the western North Pacific Ocean about ten months after the Fukushima Dai-ichi Nuclear Power Plant accident. J. Environ. Radioact. 140, 114–122. https://doi.org/10.1016/j.jenvrad.2014.11.010.

Kumamoto, Y., Yamada, M., Aoyama, M., Hamajima, Y., Kaeriyama, H., Nagai, H., Yamagata, T., Murata, A., Masumoto, Y., 2019. Radiocesium in North Pacific coastal and offshore areas of Japan within several months after the Fukushima accident. J. Environ. Radioact. 198, 79–88. https://doi.org/10.1016/j.jenvrad.2018.12.015.

Kurosawa, K., Uchiyama, Y., Kosako, T., 2020. Development of a numerical marine weather routing system for coastal and marginal seas using regional oceanic and atmospheric simulations. Ocean Eng. 195, 106706. https://doi.org/10.1016/j.oceaneng.2019.106706.

Marchesiello, P., McWilliams, J.C., Shchepetkin, A., 2003. Equilibrium structure and dynamics of the California Current system. J. Phys. Oceanogr. 33 (4), 753–783. https://doi.org/10.1175/1520-0485(2003)33<753:ESADOT>2.0.CO;2.

Mason, E., Molemaker, J., Shchepetkin, A.F., Colas, F., McWilliams, J.C., Sangrà, P., 2010. Procedures for offline grid nesting in regional ocean models. Ocean Modell. 35 (1–2), 1–15. https://doi.org/10.1016/j.ocemod.2010.05.007.

Masunaga, E., Uchiyama, Y., Suzue, Y., Yamazaki, H., 2018. Dynamics of internal tides over a shallow ridge investigated with a high-resolution downscaling regional ocean model. Geophys. Res. Lett. 45 (8), 3550–3558. https://doi.org/10.1002/2017GL076916.

Masunaga, E., Uchiyama, Y., Yamazaki, H., 2019. Strong internal waves generated by the interaction of the Kuroshio and tides over a shallow ridge. J. Phys. Oceanogr. 49 (11), 2917–2934 (pdf).

Misumi, K., Tsumune, D., Tsubono, T., Tateda, Y., Aoyama, M., Kobayashi, T., Hirose, K., 2014. Factors controlling the spatiotemporal variation of 137Cs in seabed sediment off the Fukushima coast: implications from numerical simulations. J. Environ. Radioact. 136, 218–228. https://doi.org/10.1016/j.jenvrad.2014.06.004.

Miyazawa, Y., Zhang, R., Guo, X., Tamura, H., Ambe, D., Lee, J.S., Okuno, A., Yoshinari, H., Setou, T., Komatsu, K., 2009. Water mass variability in the western North Pacific detected in a 15-year eddy resolving ocean reanalysis. J. Oceanogr. 65 (6), 737–756. https://doi.org/10.1007/s10872-009-0063-3.

Murota, K., Saito, T., Tanaka, S., 2016. Desorption kinetics of cesium from Fukushima soils. J. Environ. Radioact. 153, 134–140. https://doi.org/10.1016/j.jenvrad.2015.12.013.

Nagao, S., Kanamori, M., Ochiai, S., Tomihara, S., Fukushi, K., Yamamoto, M., 2013. Export of 134Cs and 137Cs in the Fukushima river systems at heavy rains by Typhoon Roke in September 2011. Biogeosciences 10 (10), 6215–6223. https://doi.org/10.5194/bg-10-6215-2013.

Nagao, S., Kanamori, M., Ochiai, S., Inoue, M., Yamamoto, M., 2015. Migration behavior of 134Cs and 137Cs in the Niida River water in Fukushima Prefecture, Japan during 2011–2012. J. Radioanal. Nucl. Chem. 303 (2), 1617–1621. https://doi.org/10.1007/s10967-014-3686-9.

Nakao, A., Funakawa, S., Kosaki, T., 2009. Hydroxy-Al polymers block the frayed edge sites of illitic minerals in acid soils: studies in southwestern Japan at various weathering stages. Eur. J. Soil Sci. 60 (1), 127–138. https://doi.org/10.1111/j.1365-2389.2008.01097.x.

Narimatsu, Y., Sohtome, T., Yamada, M., Shigenobu, Y., Kurita, Y., Hattori, T., Inagawa, R., 2015. Why do the radionuclide concentrations of Pacific cod depend on the body Size? In: Nakata, K., Sugisaki, H. (Eds.), Impacts of the Fukushima Nuclear Accident on Fish and Fishing Grounds. Springer, Tokyo, pp. 123–138 https://doi.org/10.1007/978-4-431-55537-7_10

Naulier, M., Eyrolle-Boyer, F., Boyer, P., Métivier, J.M., Onda, Y., 2017. Particulate organic matter in rivers of Fukushima: an unexpected carrier phase for radiocesiums. Sci. Total Environ. 579, 1560–1571. https://doi.org/10.1016/j.scitotenv.2016.11.165.

Nelson, J.M., Shimizu, Y., Abe, T., Asahi, K., Gamou, M., Inoue, T., Iwasaki, T., Kakinuma, T., Kawamura, S., Kimura, I., Kyuka, T., McDonald, R.R., Nabi, M., Nakatsugawa, M., Simões, F.R., Takebayashi, H., Watanabe, M., 2016. The international river interface cooperative: public domain flow and morphodynamics software for education and applications. Adv. Water Resour. 93, 62–74. https://doi.org/10.1016/j.advwatres.2015.09.017.

Onda, Y., Taniguchi, K., Yoshimura, K., Kato, H., Takahashi, J., Wakiyama, Y., Coppin, F., Smith, H., 2020. Radionuclides from the Fukushima Daiichi Nuclear Power Plant in terrestrial systems. Nat. Rev. Earth Environ. 1, 644–660. https://doi.org/10.1038/s43017-020-0099-x.

Qin, H., Yokoyama, Y., Fan, Q., Iwatani, H., Tanaka, K., Sakaguchi, A., Kanai, Y., Zhu, J.M., Onda, Y., Takahashi, Y., 2012. Investigation of cesium adsorption on soil and sediment samples from Fukushima Prefecture by sequential extraction and EXAFS technique. Geochem. J. 46 (4), 297–302. https://doi.org/10.2343/geochemj.2.0214.

Sakuma, K., Nakanishi, T., Yoshimura, K., Kurikami, H., Nanba, K., Zheleznyak, M., 2019. A modeling approach to estimate the 137Cs discharge in rivers from immediately after the Fukushima accident until 2017. J. Environ. Radioact. 208–209, 106041. https://doi.org/10.1016/j.jenvrad.2019.106041.

Shchepetkin, A.F., McWilliams, J.C., 2005. The regional oceanic modeling system (ROMS): a split-explicit, free-surface, topography-following-coordinate oceanic model. Ocean Modell. 9 (4), 347–404. https://doi.org/10.1016/j.ocemod.2004.08.002.

Shchepetkin, A.F., McWilliams, J.C., 2009. Computational kernel algorithms for fine-scale, multiprocess, longtime oceanic simulations. 14, 121–183. https://doi.org/10.1016/S1570-8659(08)01202-0.

Shimizu, Y.H., Takebayashi, T.I., Hamaki, M., Iwasaki, T., Nabi, M., 2014. Nays2DH solver manual. [Internet] [cited 2021 October 9]. Available from http://i-ric.org/en.

Shimizu, Y., Nelson, J., Arnez, K.F., Asahi, K., Giri, S., Inoue, T., Iwasaki, T., Jang, C.L., Kang, T., Kimura, I., Kyuka, T., Mishra, J., Nabi, M., Patsinghasanee, S., Yamaguchi, S., 2019. Advances in computational morphodynamics using the International River Interface Cooperative (iRIC) software. Earth Surf. Process. Landforms 45, 11–37. https://doi.org/10.1002/esp.4653.

Tada, H., Uchiyama, Y., Masunaga, E., 2018. Deep Sea Res. I 132, 80–93. https://doi.org/10.1016/j.dsr.2017.12.007.

Takata, H., Hasegawa, K., Oikawa, S., Kudo, N., Ikenoue, T., Isono, R.S., Kusakabe, M., 2015. Remobilization of radiocesium on riverine particles in seawater: the contribution of desorption to the export flux to the marine environment. Mar. Chem. 176, 51–63. https://doi.org/10.1016/j.marchem.2015.07.004.

Takata, H., Aono, T., Aoyama, M., Inoue, M., Kaeriyama, H., Suzuki, S., Tsuruta, T., Wada, T., Wakiyama, Y., 2020. Suspended particle-water interactions increase dissolved 137Cs activities in the nearshore seawater during Typhoon Hagibis. Environ. Sci. Technol. 54 (17), 10678–10687. https://doi.org/10.1021/acs.est.0c03254.

Takeda, N., Kashima, M., Odani, S., Uchiyama, Y., Kamidaira, Y., Mitarai, S., 2021. Identification of coral spawn source areas around the Sekisei Lagoon for recovery and poleward habitat migration by using a particle-tracking model. Sci. Rep. 11, 6963. https://doi.org/10.1038/s41598-021-86167-5.

TEPCO (Tokyo Electric Power Co.), 2012. TEPCO news press releases. [Internet];2012 (May 24) [cited 2021 October 9]. Available from https://www.tepco.co.jp/en/press/corp-com/release/2012/1204659_1870.

Tsuboi, J., Abe, S., Fujimoto, K., Kaeriyama, H., Ambe, D., Matsuda, K., Enomoto, M., Tomiya, A., Morita, T., Ono, T., Yamamoto, S., Iguchi, K., 2015. Exposure of a herbivorous fish to 134Cs and 137Cs from the riverbed following the Fukushima disaster. J. Environ. Radioact. 141, 32–37. https://doi.org/10.1016/j.jenvrad.2014.11.012.

Tsumune, D., Tsubono, T., Aoyama, M., Hirose, K., 2012. Distribution of oceanic 137Cs from the Fukushima Dai-ichi Nuclear Power Plant simulated numerically by a regional ocean model. J. Environ. Radioact. 111, 100–108. https://doi.org/10.1016/j.jenvrad.2011.10.007.

Tsumune, D., Tsubono, T., Aoyama, M., Uematsu, M., Misumi, K., Maeda, Y., Yoshida, Y., Hayami, H., 2013. One-year, regional-scale simulation of 137Cs radioactivity in the ocean following the Fukushima Daiichi Nuclear Power Plant accident. Biogeosci. Discuss. 10 (8), 5601–5617. https://doi.org/10.5194/bg-10-5601-2013.

Tsumune, D., Tsubono, T., Misumi, K., Tateda, Y., Toyoda, Y., Onda, Y., Aoyama, M., 2020. Impacts of direct release and river discharge on oceanic 137Cs derived from the Fukushima Dai-ichi Nuclear Power Plant accident. J. Environ. Radioact. 214–215, 106173. https://doi.org/10.1016/j.jenvrad.2020.106173.

Uchiyama, Y., McWilliams, J.C., Shchepetkin, A.F., 2010. Wave-current interaction in an oceanic circulation model with a vortex-force formalism: application to the surf zone. Ocean Modell. 34 (1–2), 16–35. https://doi.org/10.1016/j.ocemod.2010.04.002.

Uchiyama, Y., McWilliams, J.C., Akan, C., 2017a. Three-dimensional transient rip currents: bathymetric excitation of low-frequency intrinsic variability. J. Geophys. Res. Oceans 122, 5826–5849. https://doi.org/10.1002/2017JC013005.

Uchiyama, Y., Suzue, Y., Yamazaki, H., 2017b. Eddy-driven nutrient transport and associated upper-ocean primary production along the Kuroshio. J. Geophys. Res. Oceans 122 (6), 5046–5062. https://doi.org/10.1002/2017JC012847.

Uchiyama, Y., Kanki, R., Takano, A., Yamazaki, H., Miyazawa, Y., 2018a. Mesoscale reproducibility in regional ocean modeling with a 3-D stratification estimate based on Aviso-Argo data. 55, 1–18. https://doi.org/10.1080/07055900.2017.1399858.

Uchiyama, Y., Zhang, X., Suzue, Y., Kosako, T., Miyazawa, Y., Nakayama, A., 2018b. Residual effects of treated effluent diversion on a seaweed farm in a tidal strait using a multi-nested high-resolution 3-D circulation-dispersal model. Mar. Pollut. Bull. 130, 40–54. https://doi.org/10.1016/j.marpolbul.2018.03.007.

Uchiyama, Y., Odani, S., Kashima, M., Kamidaira, Y., Mitarai, S., 2018c. Influences of the Kuroshio on interisland remote connectivity of corals across the Nansei Archipelago in the East China Sea. J. Geophys. Res. Oceans 123 (12), 9245–9265. https://doi.org/10.1029/2018JC014017.

Ueda, S., Hasegawa, H., Kakiuchi, H., Akata, N., Ohtsuka, Y., Hisamatsu, S.I., 2013. Fluvial discharges of radiocaesium from watersheds contaminated by the Fukushima Daiichi Nuclear Power Plant accident,Japan. 118, 96–104. https://doi.org/10.1016/j.jenvrad.2012.11.009.

Wada, T., Nemoto, Y., Shimamura, S., Fujita, T., Mizuno, T., Sohtome, T., Kamiyama, K., Morita, T., Igarashi, S., 2013. Effects of the nuclear disaster on marine products in Fukushima. J. Environ. Radioact. 124, 246–254. https://doi.org/10.1016/j.jenvrad.2013.05.008.

Yamashiki, Y., Onda, Y., Smith, H.G., Blake, W.H., Wakahara, T., Igarashi, Y., Matsuura, Y., Yoshimura, K., 2014. Sci. Rep. 4 (1), 3714. https://doi.org/10.1038/srep03714.

Yasunari, T.J., Stohl, A., Hayano, R.S., Burkhart, J.F., Eckhardt, S., Yasunari, T., 2011. Cesium-137 deposition and contamination of japanese soils due to the Fukushima nuclear accident. Proc. Natl. Acad. Sci. U. S. A. 108 (49), 19530–19534. https://doi.org/10.1073/pnas.1112058108.

Zhang, X., Uchiyama, Y., Nakayama, A., 2019. On relaxation of the influences of treated sewage effluent on an adjacent seaweed farm in a tidal strait. Mar. Pollut. Bull. 144, 265–274. https://doi.org/10.1016/j.marpolbul.2019.04.050.